# Conductivity control via minimally invasive anti-Frenkel defects in a functional oxide

Donald M. Evans[1,*], Theodor S. Holstad[1,*], Aleksander B. Mosberg[2,*], Didrik R. Småbråten[1,*], Per Erik Vullum[3], Anup L. Dadlani[4], Konstantin Shapovalov[5], Zewu Yan[6,7], Edith Bourret[7], David Gao[2,8], Jaakko Akola[2,9], Jan Torgersen[4], Antonius T. J. van Helvoort[2], Sverre M. Selbach[1], and Dennis Meier[1]

*The authors contributed equally

Email: donald.evans@ntnu.no; dennis.meier@ntnu.no

[1]Department of Materials Science and Engineering, Norwegian University of Science and Technology (NTNU), 7491 Trondheim, Norway

[2]Department of Physics, Norwegian University of Science and Technology (NTNU), 7491 Trondheim, Norway

[3]SINTEF Industry, 7491 Trondheim, Norway

[4]Deparment of Mechanical and Industrial Engineering, Norwegian University of Science and Technology (NTNU), 7491 Trondheim, Norway

[5]Institut de Ciència de Materials de Barcelona (ICMAB-CSIC), Campus UAB, 08193 Bellaterra, Spain

[6]Department of Physics, ETH Zurich, 8093 Zürich, Switzerland

[7]Materials Sciences Division, Lawrence Berkeley National Laboratory, Berkeley, California 94720, USA

[8]Nanolayers Research Computing LTD, 1 Granville Ct, London, N12 0HL, UK

[9]Computational Physics Laboratory, Tampere University, 33014 Tampere, Finland

**Utilizing quantum effects in complex oxides, such as magnetism, multiferroicity and superconductivity, requires atomic-level control of the material`s structure and composition. In contrast, the continuous conductivity changes that enable artificial oxide-based synapses and multi-configurational devices, are driven by redox reactions and domain reconfigurations, entailing long-range ionic migration and changes in stoichiometry or structure. While both concepts hold great technological potential, combined applications seem difficult due to the mutually exclusive requirements. Here, we demonstrate a route to overcome this limitation by controlling the conductivity in the functional oxide hexagonal $Er(Mn,Ti)O_3$, by using conductive Atomic Force Microscopy (AFM) to generate electric-field induced anti-Frenkel defects, that is, charge-neutral anion interstitial-vacancy pairs. These defects are generated with nanoscale spatial precision, where they locally enhance electronic hopping conductivity by orders of magnitude without disturbing the ferroelectric order. We explain the non-volatile effects using density functional theory and discuss its universality, suggesting an alternative dimension to functional oxides and the development of multifunctional devices for next-generation nanotechnology.**

A continuous range of conductivity levels in oxide materials can enable innovative technologies such as multilevel data storage in memristor chips and synaptic devices for neuromorphic computing[1–4]. Different mechanisms[5,6] are now established that allow for tuning the conductivity in oxides gradually and by multiple orders of magnitude[7]. For example, electric fields modify the n-type conductivity in $LaAlO_3$-$SrTiO_3$ heterostructures[8] and multiferroic ($BiFeO_3$)[9] thin films, which has been explained based on the creation and migration of positively charged oxygen vacancies ($v_O^{\bullet\bullet}$). In addition, migration of negatively charged oxygen interstitials ($O_i''$) has been exploited to control the p-type conductivity in hexagonal $Y_{0.67}Lu_{0.33}MnO_3$ single crystals[10]. However, both the migration of $v_O^{\bullet\bullet}$ and $O_i''$ are aspects of the same phenomenon, that is, an electric-field driven redox reaction of a transition metal oxide. While these redox reactions give the desired conductivity changes, the creation of either $v_O^{\bullet\bullet}$ or $O_i''$ necessarily alters the overall stoichiometry in the host material, too, with significant impact on the material's spin, charge and orbital degrees of freedom. The latter is reflected by the sensitivity of oxides towards variations in stoichiometry, which can drive systems between metallic and insulating states[11], stabilize superconductivity[12], or completely suppress magnetic[13] and electric order[14,15]. In general, the long-range migration and extraction/injection of ions associated with currently applied redox reactions induces a net mass transport giving rise to chemical, electrostatic, and strain-related gradients.[2,14,16] This prohibits utilization in parallel with emergent electronic functionalities beyond merely conductivity.

In order to avoid detrimental side-effects and ultimately use the full range of functional properties available in oxide materials, a conceptually different approach for controlling conductivity is needed. Particularly promising are stoichiometric defects as classically reported, for example, in ionic fluorites[15]. Here, anions move from lattice sites to interstitial positions, forming entropy-stabilized and charge-neutral interstitial-vacancy pairs (anti-Frenkel defects[15]). While in electroceramics it is clear that intrinsic anti-Frenkel defects play a key role for the ionic-electronic transport, their utilization for controlling conductivity in correlated oxides remains unexplored. Most

studies in the field of oxide electronics focus on systems from the large family of perovskite materials, which are unlikely to form anti-Frenkel defects due to their rather dense crystal structure. As a consequence, fundamental aspects, such as their creation, stability and impact on functionalities other than mixed ionic-electronic transport, fall into largely uncharted territory.

In this study, we work with the ferroelectric p-type semiconductor $ErMnO_3$ (single-crystals, see Methods) from the family of hexagonal (h-) manganites with 0.2% Ti-doping (denoted h-$Er(Mn,Ti)O_3$ in the following). The applied Ti-doping lowers the conductivity, $\sigma_{dc}$(h-$Er(Mn,Ti)O_3$) = 2.6 x $10^{-8}$ $\Omega^{-1}$ $cm^{-1}$, compared to $\sigma_{dc}$(h-$ErMnO_3$) = 2.5 x $10^{-7}$ $\Omega^{-1}$ $cm^{-1}$ for the undoped sample[17]. Aside from its semiconducting properties, h-$Er(Mn,Ti)O_3$ exhibits a spontaneous polarization along its [001]-axis ($P \approx 5.5$ µC $cm^{-2}$), which emerges at $T_c \approx 1470$ K driven by a tripling of the structural unit cell[18–20]. Importantly, the structure of hexagonal manganites is about 11% less dense than the corresponding orthorhombic perovskite structure, and $v_O^{\bullet\bullet}$ and $O_i''$ are equally important for the electronic properties[21,22]. In addition, such defects are already mobile below 200 °C, whereas cations migrate only above 800 °C, which enables anion-defect driven electronic property control[23,24].

**Local control of electrical conductance**

Figure 1a presents the distribution of ferroelectric 180° domains in h-$Er(Mn,Ti)O_3$ acquired by piezoresponse force microscopy (PFM) on a sample with in-plane polarization ([110] orientation, see Methods). Figure 1b shows a representative conductance map, gained by conductive atomic force microscopy (cAFM) using a conducting probe-tip (curvature radius ≈ 100 nm) after writing a network of wires with negative voltage, $U^{write} = -8$ V, applied to the back electrode. The image is recorded with a positive voltage, $U^{read} = +10$ V, showing different wires with a width of about 100 nm and enhanced conductance compared to the surrounding material. The effect is equally pronounced in $\pm P$ domains and occurs on both surfaces with in-plane $P$ (Fig. 1b) and surfaces with out-of-plane $P$ (inset to Fig. 1c).

We note that this is qualitatively different from the $O_i''$-migration-induced changes in conductance in h-$Y_{0.67}Lu_{0.33}MnO_3$, which were reported to occur under comparable conditions but only on surfaces with in-plane *P*.[10] Importantly, we find that the enhanced conductance of our electric-field induced features persists on the time scale of years under ambient conditions (see Fig. 1c), and no signature of degradation is observed up to 105 °C (Supplementary Fig. S1). A reset to the original state is possible by annealing at 300 °C, reflecting a barrier for stability in the order of 0.035 to 0.050 eV (Fig. S2). Furthermore, and in contrast to previous AFM-written conducting nano-features in $LaAlO_3$-$SrTiO_3$[8,25] that rely on hydrogen ($H^+$) penetration, our structures are robust against solvents, such as acetone, ethanol, and methanol. In fact, we do not observe qualitative differences between writing conducting features in air (ambient) and under nitrogen atmosphere (Fig. S3), which discards $H^+$ penetration as the driving force behind the change in conductivity. The conclusion that neither only $O_i''$ nor $H^+$ is responsible for the enhanced conductance is corroborated by time- and voltage-dependent studies (Fig. S4), as well as local transport measurements (Fig. S5), which cannot be explained by only one type of defect. To quantify the induced changes in conductivity and to analyse the influence of the polarity (+ or −) and size of the applied voltage, we draw a series of boxes (see inset to Fig. 1d), systematically varying the write voltage $U^{write}$ from −10 V to +10 V. The impact of the varying $U^{write}$ is then monitored by cAFM scans taken with a positive voltage of +10 V. The results are summarized in Fig. 1d, which shows the averaged measured current, $I^{read}$, as function of $U^{write}$. Figure 1d reveals that $I^{read}$ depends on the polarity of the write voltage: for negative voltages exceeding −5 V, we observe an increase in the conductance by about three orders of magnitude. In contrast, positive voltages do not lead to an increase in the conductance, consistent with the formation of a Schottky barrier at the tip-sample interface.[10,26] The latter is also confirmed by separate experiments at higher voltages up to +60 V (see Fig. S6). Thus, the experiments demonstrate that conducting features can be written with negative voltages ($U^{write} \lesssim -5$ V) and read-out by positive voltages ($0 < U^{read} \lesssim +60$ V). By writing features of different shapes (wires and dots), we can achieve an enhancement of up to four orders of magnitude in $I^{read}$ without significant changes in surface topography (see Supplementary Fig. S7 and

S8). The data demonstrates that localized electric fields can enhance the conductance in h-Er(Mn,Ti)$O_3$ by up to four orders of magnitude; the changes are durable, resistant to moderate heating and chemical solvents, and can be induced with nanometer spatial precision.

**3D morphology and structural properties**

To understand the origin of the enhanced conductance, we investigate how the effect evolves within the bulk. Figure 2a and inset show a comparison of scanning electron microscopy (SEM) and cAFM images from the same area, revealing an elliptically shaped bright area that has been written with $U^{write} = -60$ V applied for 5 s. A comparison of the SEM and cAFM data shows that bright contrast in SEM correlates with high conductivity. This correlation allows us to evaluate how the electric-field induced changes protrude into the depth of the sample based on SEM images. For this purpose, we take a cross-sectional images from the region of interest (Fig. 2b), using a dual beam focused ion beam (FIB)-SEM (see Methods). Consistent with our AFM data (Fig. S8), the cross-sectional SEM images show no significant change in surface topography. Instead, Figure 2b reveals that the region of enhanced conductance extends more than 0.5 μm into the depth of the sample. A schematic 3D reconstruction of the conducting area based on the SEM data is presented in Fig. 2c. This distribution is consistent with the anisotropic behaviour observed in the electronic transport[27] and the ionic mobility in the hexagonal manganites (Supplementary Fig. S9), indicating that the changes that give rise to enhanced conductance are a bulk phenomenon rather than a surface effect.

To test for related structural modifications in the bulk, we take high-angle annular dark field scanning transmission electron microscopy (HAADF-STEM) lattice images inside and away from the conducting region in Fig. 2b. Figure 2d and 2e present HAADF-STEM scans viewed down the [$\bar{1}$ 0 0] direction, comparing the electrically modified region to the as-grown structure, respectively. The images represent the typical up-up-down pattern of Er atoms[28], separated by layers of Mn atoms.

Interestingly, both real and reciprocal space investigations show no differences in positions between the two regions (see Fig. 2d and 2e, and insets). In particular, when analysing the arrangement of Er atoms, we find no statistically significant decrease in Er displacement within the conductive region, or modification of the unit cell size (Supplementary Fig. S10), suggesting that the driving mechanism for enhanced conductivity is due to subtle effects related to the local electronic structure. Furthermore, as the improper electric polarization in h-Er(Mn,Ti)$O_3$ arises from the Er displacement[29–32], its robustness demonstrates that the orientation and magnitude of the ferroelectric order is unaffected by the electric-field induced increase in conductance (Fig. 2a,b).

**Electrochemical structure and electric-field induced modifications**

We next analyse the electronic structure at the local scale, using electron energy-loss spectroscopy (EELS). Figure 3a displays averaged EELS spectra showing the Mn $L_{2,3}$-edge in the bulk (blue) and the modified conducting region (yellow). A comparison of the EELS data reveals changes in spectral weight, whereas the $L_3/L_2$ white-line intensity ratio remains constant, suggesting that the net Mn oxidation state is preserved. We demonstrate the reproducibility of this subtle effect by recording EELS spectra at the Mn $L_{2,3}$-edge from a second line scan in different positions, which leads to qualitatively equivalent results (see Fig. S11). To evaluate the detected change, we follow the approach used in ref. [33–37] and fit the full Mn $L_{2,3}$-edge with three spectra, corresponding to $Mn^{2+}$ and $Mn^{4+}$ spectra from literature[37] and experimental reference spectra recorded away from the conducting region. This procedure allows for quantifying relative changes with respect to the bulk even without knowing the exact defect density in the as-grown state (note that bulk h-Er(Mn,Ti)$O_3$ displays p-type conductivity, which implies the presence of $O_i''$, Fig. S5). We find that linear combinations of two spectra (bulk and $Mn^{2+}$, or bulk and $Mn^{4+}$) alter the peak form and $L_3/L_2$ white-line intensity ratio, making it unlikely that only one defect type (either $v_O^{\bullet\bullet}$ or $O_i''$) is responsible for the experimentally observed change in spectral weight (see Supplementary Fig. S11 and S12 for details).

In contrast, assuming an equal concentration of $Mn^{2+}$ and $Mn^{4+}$, we can reproduce the averaged EELS spectra for the Mn $L_{2,3}$-edge in the conducting regime (red lines in Fig. 3(a), Fig. S10 and S12), suggesting a coexistence of $v_O^{\bullet\bullet}$ and $O_i''$. The latter is consistent with the formation of ($v_O^{\bullet\bullet}$, $O_i''$) defect pairs, i.e., anti-Frenkel defects[15]. On the basis of our fits, we calculate an increase of about 3.25 ± 0.5 % in the concentration of $Mn^{4+}$ and $Mn^{2+}$ relative to the bulk, corresponding to about one anti-Frenkel defect for every ninth unit cells (Supplementary Fig. S12).

To find additional evidence, we consider EELS spectra taken at the O K-edge in the bulk (Fig. 3b) and in the conducting region (Fig. 3c) and apply the *ab initio* self-consistent multiple-scattering code FEFF[38] to analyse emergent site-specific differences for the four symmetrically inequivalent oxygen positions[19] in h-Er(Mn,Ti)$O_3$ (see inset to Fig. 3a). Representative calculated spectra for apical (O1 and O2) and planar (O3) oxygen are given as insets to Fig. 3b and c, respectively. For the bulk, the spectra calculated for apical oxygen in an oxygen stoichiometric system adequately replicate the main features of the O K-edge, labelled ① to ⑤ (an overview of all oxygen spectra is given in Fig. S13). In contrast, in the conducting region (yellow in Fig. 3c) the O K-edge shows several differences compared to the bulk, including the emergence of a distinct peak at about 537 eV, which can no longer be explained based on apical oxygen alone. At this energy, however, a peak is present in the calculated spectra for planar oxygen (O3, black line), which is expected to have an increased contribution in the presence of anti-Frenkel defects due to changes in the oxygen bond angle (see inset to Fig. 3c for an illustration). Although the O K-edge results are in tune with the data gained at the Mn $L_{2,3}$-edge and consistent with the formation of anti-Frenkel defects, from the spectroscopy data alone one cannot unambiguously conclude a coexistence of both $v_O^{\bullet\bullet}$ and $O_i''$. Direct evidence of this coexistence is provided, however, by the time- and voltage-dependent study in Fig. S4, showing a separation of positively ($v_O^{\bullet\bullet}$) and negatively ($O_i''$) charged defects under longer exposure to electric fields.

**Stability and electronic properties of anti-Frenkel defects**

To develop a microscopic model, we apply first principles calculations based on density functional theory (DFT) using the isostructural compound h-$YMnO_3$ as model system (Methods; analogous to ref. [33] the calculations are performed for h-$YMnO_3$, which is structurally and electronically similar to h-$ErMnO_3$, but the absence of f-electrons simplifies the DFT description). We find that $O_i''$ (locally contracting the lattice[21]) and $v_O^{\bullet\bullet}$ (locally expanding the lattice[39]) are structurally screened and, hence, do not recombine when they are more than ≈6 Å apart. Instead, at $T$ = 0 K, they form an electrically compensated meta-stable anti-Frenkel defect ($v_O^{\bullet\bullet}$, $O_i''$) as sketched in Fig. 4a (see Supplementary Notes 1 and 2, and Supplementary Fig. S14 and Supplementary Fig. S15 for details). These defects cause a change in the electronic DOS compared to the stoichiometric unit, Fig. 4b, as illustrated in Fig. 4c. To gain insight into the defect structure at finite temperature and analyse its stability, we perform molecular dynamic (MD) simulations at 300 K, 573 K, and 1000 K (see Supplementary Information). The MD simulations reveal that the system can slightly lower its energy by forming $O_i''$-dimers, subtly modifying the basic anti-Frenkel defect structure in Fig. 4a (see Fig. S16 for an illustration). The modified anti-Frenkel defect exhibits a DOS comparable to Fig. 4c and, importantly, does not recombine at 300 K and 573 K within 5 ps and 10 ps trajectories, respectively. In contrast, at 1000 K we observe recombination within 3 ps, confirming that recombination occurs at sufficiently high temperature.

The higher conductance in regions with enhanced anti-Frenkel defect density can be understood from the calculated electronic density of states (DOS) and the corresponding simplified band structure in Fig. 4c (see Fig. S17 for the site-specific DOS). In general, electrical transport in h-$Er(Mn,Ti)O_3$ occurs via hopping conductivity, reported as Poole-Frenkel conduction[17], and the same mechanism is observed in the modified region (Fig. S18). Figure 4c shows that both the number of charge carriers and defect sites available for hopping increase, explaining the observed higher hopping conductivity. The electron-hole pairs associated with anti-Frenkel defects may recombine and give rise

to an electrically uncompensated charge state of the anti-Frenkel defect. However, the latter is energetically costly so that new charge carriers would be created to replace the missing electron-hole pair and move the system back to equilibrium (Fig. S15).

**Outlook**

The electric-field induced anti-Frenkel defects studied in this work thus enable minimally invasive and non-volatile conductivity control with nanoscale spatial precision. Importantly, the emergence of parasitic chemical, electrostatic, and strain-related gradients associated with conventional approaches is avoided and the material`s overall stoichiometry is preserved. Anti-Frenkel defects can be applied in any system that can stably compensate multiple oxygen stoichiometries, such as the families of hexagonal rare-earth gallates and indates[40], hexaferrite[41], fluorites[42], Ruddlesdon-Popper[43] systems as well as tungsten bronzes. Here, – analogous to the hexagonal manganites – their controlled creation via electric fields is likely, allowing to increase the density of defect sites and enhance hopping conductivity. With this, a new generation of multifunctional oxides becomes possible in which multilevel conductivity control can be utilized in parallel with phenomena such as ferroelectricity, magnetism, and superconductivity without changing the electronic interactions that control them.

## References


1. Seok Jeong, D., Kim, I., Ziegler, M. & Kohlstedt, H. Towards artificial neurons and synapses: A materials point of view. *RSC Adv.* **3**, 3169–3183 (2013).

2. Ielmini, D. & Wong, H. S. P. In-memory computing with resistive switching devices. *Nat. Electron.* **1**, 333–343 (2018).

3. Del Valle, J., Ramírez, J. G., Rozenberg, M. J. & Schuller, I. K. Challenges in materials and devices for resistive-switching-based neuromorphic computing. *J. Appl. Phys.* **124**, 211101 (2018).

4. Chanthbouala, A. *et al.* A ferroelectric memristor. *Nat. Mater.* **11**, 860–864 (2012).

5. Hwang, H. Y. *et al.* Emergent phenomena at oxide interfaces. *Nat. Mater.* **11**, 103–113 (2012).

6. Ramesh, R. & Schlom, D. G. Creating emergent phenomena in oxide superlattices. *Nat. Rev. Mater.* **4**, 257–268 (2019).

7. Lee, J. S., Lee, S. & Noh, T. W. Resistive switching phenomena: A review of statistical physics approaches. *Appl. Phys. Rev.* **2**, 31303 (2015).

8. Cen, C. *et al.* Nanoscale control of an interfacial metal–insulator transition at room temperature. *Nat. Mater.* **7**, 298–302 (2008).

9. Du, N. *et al.* Field-Driven Hopping Transport of Oxygen Vacancies in Memristive Oxide Switches with Interface-Mediated Resistive Switching. *Phys. Rev. Appl.* **10**, 54025 (2018).

10. Wang, X. *et al.* Anisotropic resistance switching in hexagonal manganites. *Phys. Rev. B* **99**, 054106 (2019).

11. Nagarajan, L. *et al.* A chemically driven insulator-metal transition in non-stoichiometric and amorphous gallium oxide. *Nat. Mater.* **7**, 391–398 (2008).

12. Cava, R. J. *et al.* Oxygen stoichiometry, superconductivity and normal-state properties of $YBa_2Cu_3O_{7-\delta}$. *Nature* **329**, 423–425 (1987).

13. Zhao, J. *et al.* Lattice and magnetic structures of PrFeAsO, $PrFeAsO_{0.85}F_{0.15}$, and $PrFeAsO_{0.85}$. *Phys. Rev. B* **78**, 132504 (2008).

14. Kalinin, S. V., Jesse, S., Tselev, A., Baddorf, A. P. & Balke, N. The role of electrochemical phenomena in scanning probe microscopy of ferroelectric thin films. *ACS Nano* **5**, 5683–5691 (2011).

15. Joachim Maier. *Physical Chemistry of Ionic Materials*. *Ions and Electrons in Solids* (Wiley, 2004).

16. Kumar, A., Ciucci, F., Morozovska, A. N., Kalinin, S. V. & Jesse, S. Measuring oxygen reduction/evolution reactions on the nanoscale. *Nat. Chem.* **3**, 707–713 (2011).

17. Holstad, T. S. *et al.* Electronic bulk and domain wall properties in B-site doped hexagonal $ErMnO_3$. *Phys. Rev. B* **97**, 85143 (2018).

18. Chae, S. C. *et al.* Direct observation of the proliferation of ferroelectric loop domains and vortex-antivortex pairs. *Phys. Rev. Lett.* **108**, 167603 (2012).

19. Van Aken, B. B., Palstra, T. T. M., Filippetti, A. & Spaldin, N. A. The origin of ferroelectricity in magnetoelectric $YMnO_3$. *Nat. Mater.* **3**, 164–170 (2004).

20. Han, M.-G. *et al.* Ferroelectric Switching Dynamics of Topological Vortex Domains in a Hexagonal Manganite. *Adv. Mater.* **25**, 2415–2421 (2013).

21. Skjærvø, S. H. *et al.* Interstitial oxygen as a source of p-type conductivity in hexagonal manganites. *Nat. Commun.* **7**, 13745 (2016).

22. Skjærvø, S. H., Småbråten, D. R., Spaldin, N. A., Tybell, T. & Selbach, S. M. Oxygen vacancies in the bulk and at neutral domain walls in hexagonal $YMnO_3$. *Phys. Rev. B* **98**, 184102 (2018).

23. Remsen, S. & Dabrowski, B. Synthesis and oxygen storage capacities of hexagonal $Dy_{1-x}Y_xMnO_{3+\delta}$. *Chem. Mater.* **23**, 3818–3827 (2011).

24. Bergum, K. *et al.* Synthesis, structure and magnetic properties of nanocrystalline $YMnO_3$. *Dalt. Trans.* **40**, 7583–7589 (2011).

25. Bi, F. *et al.* 'Water-cycle' mechanism for writing and erasing nanostructures at the $LaAlO_3/SrTiO_3$ interface. *Appl. Phys. Lett.* **97**, 173110 (2010).

26. Schaab, J. *et al.* Electrical half-wave rectification at ferroelectric domain walls. *Nat. Nanotechnol.* **13**, 1028–1034 (2018).

27. Katsufuji, T. *et al.* Dielectric and magnetic anomalies and spin frustration in hexagonal $RMnO_3$ (*R* = Y, Yb, and Lu). *Phys. Rev. B* **64**, 104419 (2001).

28. Zhang, Q. H. *et al.* Direct observation of interlocked domain walls in hexagonal RMnO3 (R=Tm, Lu). *Phys. Rev. B* **85**, 20102 (2012).

29. Holtz, M. E. *et al.* Topological Defects in Hexagonal Manganites: Inner Structure and Emergent Electrostatics. *Nano Lett.* **17**, 5883–5890 (2017).

30. Fennie, C. J. & Rabe, K. M. Ferroelectric transition in $YMnO_3$ from first principles. *Phys. Rev. B* **72**, 100103 (2005).

31. Artyukhin, S., Delaney, K. T., Spaldin, N. A. & Mostovoy, M. Landau theory of topological defects in multiferroic hexagonal manganites. *Nat. Mater.* **13**, 42–49 (2013).

32. Cano, A. Hidden order in hexagonal $RMnO_3$ multiferroics (*R*=Dy -Lu, In, Y, and Sc). *Phys. Rev. B* **89**, 214107 (2014).

33. Mundy, J. A. *et al.* Functional electronic inversion layers at ferroelectric domain walls. *Nat. Mater.* **16**, 622–627 (2017).

34. Tan, H., Verbeeck, J., Abakumov, A. & Van Tendeloo, G. Oxidation state and chemical shift

investigation in transition metal oxides by EELS. *Ultramicroscopy* **116**, 24–33 (2012).

35. Nishida, S. *et al.* Effect of local coordination of Mn on Mn-$L_{2,3}$ edge electron energy loss spectrum. *J. Appl. Phys.* **114**, 54906 (2013).

36. Loomer, D. B., Al, T. A., Weaver, L. & Cogswell, S. Manganese valence imaging in Mn minerals at the nanoscale using STEM-EELS. *Am. Mineral.* **92**, 72–79 (2007).

37. Garvie, L. A. J. & Craven, A. J. High-resolution parallel electron energy-loss spectroscopy of Mn $L_{2,3}$-edges in inorganic manganese compounds. *Phys. Chem. Miner.* **21**, 191–206 (1994).

38. Rehr, J. J., Kas, J. J., Vila, F. D., Prange, M. P. & Jorissen, K. Parameter-free calculations of X-ray spectra with FEFF9. *Phys. Chem. Chem. Phys.* **12**, 5503–5513 (2010).

39. Overton, A. J., Best, J. L., Saratovsky, I. & Hayward, M. A. Influence of topotactic reduction on the structure and magnetism of the multiferroic $YMnO_3$. *Chem. Mater.* **21**, 4940–4948 (2009).

40. Griffin, S. M., Reidulff, M., Selbach, S. M. & Spaldin, N. A. Defect Chemistry as a Crystal Structure Design Parameter: Intrinsic Point Defects and Ga Substitution in $InMnO_3$. *Chem. Mater.* **29**, 2425–2434 (2017).

41. Zhang, X., Zhang, Y., Yue, Z. & Zhang, J. Influences of sintering atmosphere on the magnetic and electrical properties of barium hexaferrites. *AIP Adv.* **9**, 085129 (2019).

42. Keeton, S. C. & Wilson, W. D. Vacancies, interstitials, and rare gases in fluorite structures. *Phys. Rev. B* **7**, 834–843 (1973).

43. Boulahya, K., Muñoz-Gil, D., Gómez-Herrero, A., Azcondo, M. T. & Amador, U. $Eu_2SrCo_{1.5}Fe_{0.5}O_7$ a new promising Ruddlesden-Popper member as a cathode component for intermediate temperature solid oxide fuel cells. *J. Mater. Chem. A* **7**, 5601–5611 (2019).

**Acknowledgements** The authors thank Tor Grande for fruitful discussions. DRS and SMS were supported by the Research Council of Norway (project number 231430/F20 and 275139) and acknowledge UNINETT Sigma2 (Project no. NN9264K and ntnu243) for providing the computational resources. ABM was supported by NTNU's Enabling technologies: Nanotechnology. The Research Council of Norway is acknowledged for the support to the Norwegian Micro- and Nano-Fabrication Facility, NorFab, project number 245963/F50 and Norwegian Centre for Transmission Electron Microscopy, NORTEM, Grant No. 197405. ALD was funded by the Norwegian Research Council under project number 274459 Translate. ZY and EB were supported by the U.S. Department of Energy, Office of Science, Basic Energy Sciences, Materials Sciences and Engineering Division under Contract No. DE-AC02-05-CH11231 within the Quantum Materials program-KC2202. DM thanks NTNU for support through the Onsager Fellowship Programme and NTNU Stjerneprogrammet.

**Author contributions** DME coordinated the project and lead the scanning probe microscopy work together with TSH, both supervised by DM. ABM conducted the FIB and SEM work under supervision of AvH. PEV, AvH, ABM, conducted TEM and together with TSH and DME analyzed the TEM and EELS data. DRS performed the DFT calculations and ALD simulated the EELS spectra supervised by SMS and JT, respectively. KS modelled the defect segregation in electric fields. ZY and EB provided the materials and DG and JA supported the study with image charge and potential alignment correction simulations for charged defects in periodic boundary conditions. DME and DM wrote the manuscript. All authors discussed the results and contributed to the final version of the manuscript.

**Data availability** Computer codes used for simulations and data evaluation are available from the sources cited; data in other formats than presented within this paper are available from the corresponding authors upon request.

**Additional information** Supplementary information is available for this paper at https://... Reprints and permission information is available online at www.nature.com/reprints. Correspondence and requests for materials should be addressed to DME and DM.

## Figures and Figure Captions

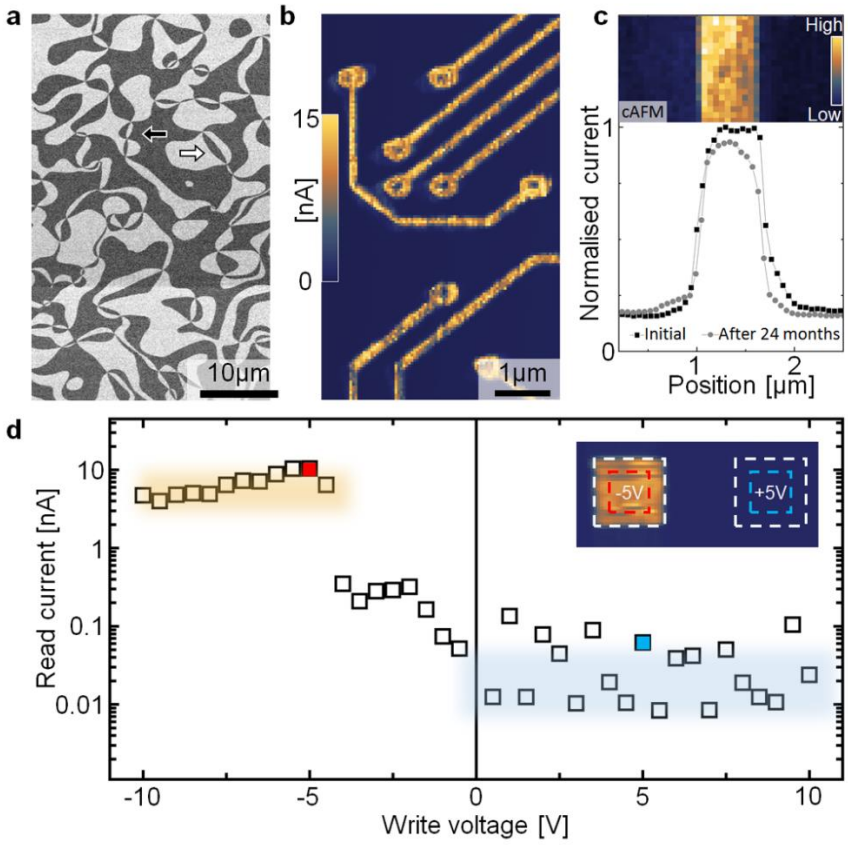


**Figure 1 | Local conductivity control in hexagonal h-Er(Mn,Ti)$O_3$. a,** Piezoresponse force microscopy (PFM, in-plane contrast) image, showing the characteristic distribution of ferroelectric domains. Arrows indicate the polarisation direction (dark, *-P* and bright, *+P*). **b,** Conductive atomic force microscopy (cAFM) scan showing conducting nano-wires (bright) on a less conducting background of both *-P* and *+P* domains similar to **a**. The image is gained with a positive bias ($U^{read}$ = +10 V) after writing wires with a negative bias of ($U^{write}$ = −8 V). Voltages are applied to the back electrode. **c,** Normalised current recorded on a conducting bar right after writing it on a sample with out-of-plane *P* and, again, 24 months later ($U^{read}$ = +12 V, $U^{write}$ = −21 V). The profiles are gained from cAFM images as shown in the inset by averaging over multiple cross sections. The curves are offset so that the background current away from the conducting feature aligns. The data reflects the long-term stability of the electric-field induced conducting features in h-Er(Mn,Ti)$O_3$. **d,** Average current measured at $U^{read}$ = +10 V from a series of 1 x 1 µm boxes written with voltages between −10 V and +10 V. Representative spatially resolved cAFM data for boxes written with ±5 V are shown in the inset. White dashed lines frame the boxes, whereas coloured dashed lines mark the areas (0.5 x 0.5 µm) over which the current is averaged to quantify the read current.

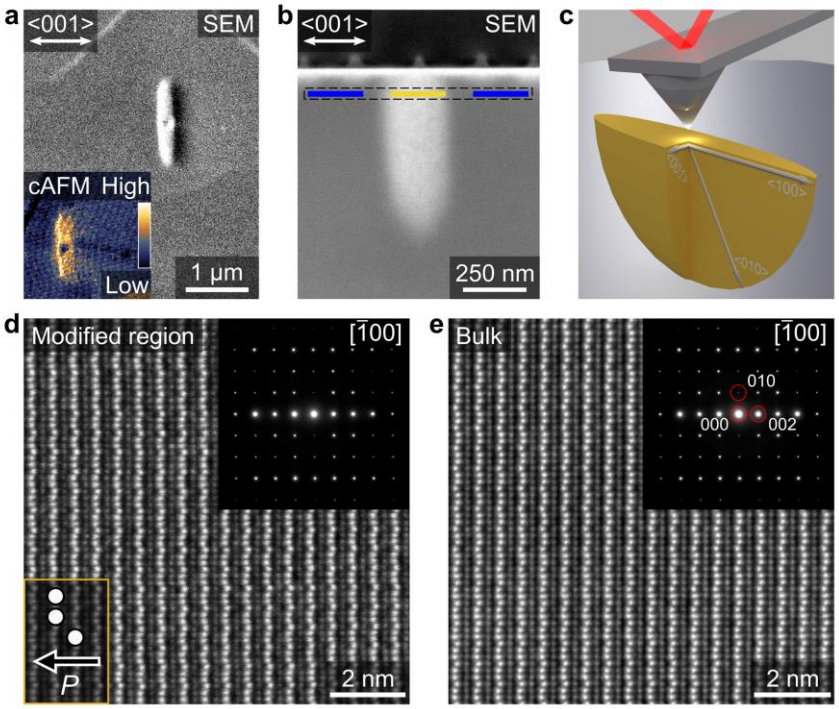


385

386 **Figure 2 | Morphology and structure of electric-field induced conducting features. a,** Top-down SEM
387 and cAFM (inset, $U^{read}$ = +45 V) image of an elliptically shaped conducting region (bright), generated
388 by applying $U^{write}$ = –60 V for 5 s, while keeping the probe tip stationary probe. The white arrow
389 indicates the ferroelectric axis (*P* || <001>). **b,** SEM image of a FIB cross-section from **a,** revealing how
390 the conducting feature protrudes into the bulk of h-Er(Mn,Ti)$O_3$ and showing where, in the final TEM
391 lamella, the EELS line scan for Fig. 3 is taken (blue and yellow represent the bulk and electrically
392 modified region, respectively). **c,** 3D sketch representing the cAFM induced conducting feature and
393 the shape dependence on crystallographic axes based on the cross section in **b** and cross sections of
394 equivalent dots taken in perpendicular directions. **d,** HAADF-STEM image from the high conductive
395 region seen in **b**, viewed along the *P*6$_3$*cm* [$\bar{1}$00] zone axis, with τ/λ = 0.40 ± 0.02. The brighter Er atomic
396 positions show the characteristic up-up-down displacement as discussed in ref. [29] and the arrow in
397 the inset shows how this links to the ferroelectric polarisation *P*. **e,** HAADF-STEM image taken in the
398 unmodified bulk region. The analysis of the crystal lattice in **d** and **e** reveals no measurable differences,
399 reflecting that the atomic scale structure and, hence, the ferroelectric polarisation, are unaffected by
400 the electric-field induced change in conductivity. Insets in (**d**, **e**) show selected area electron diffraction
401 (SAED) patterns of the corresponding regions.

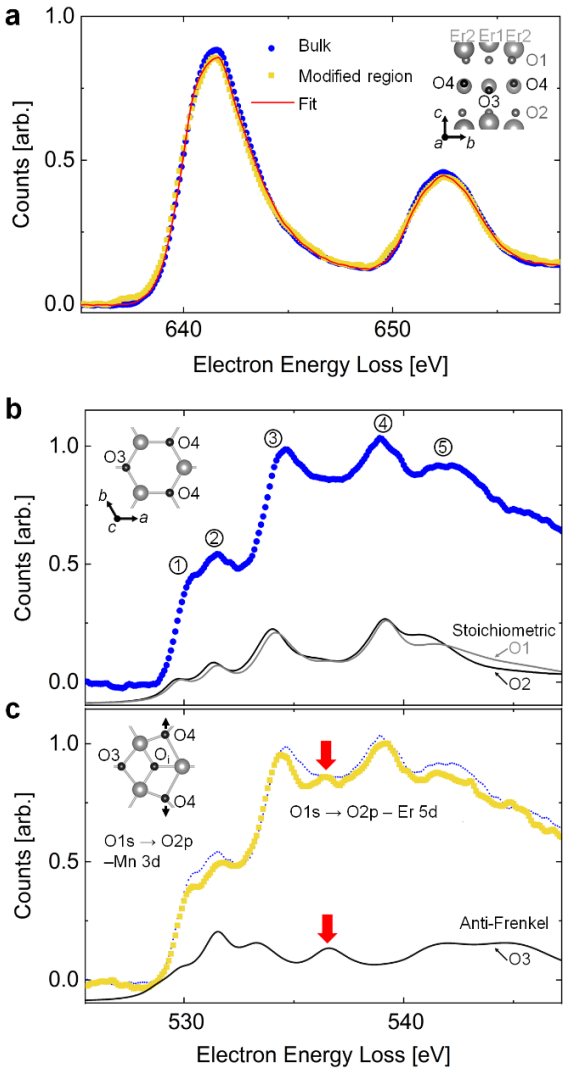


**Figure 3 | Comparison of the electronic structure in as-grown and electrically modified regions. a,** Blue and yellow data points represent EELS spectra of the Mn $L_{2,3}$ edge in h-Er(Mn,Ti)$O_3$ taken in the bulk and the modified conducting region, respectively ($t/\lambda = 0.40 \pm 0.02$). The red line is a fit to the Mn $L_{2,3}$ edge in the conducting region based on a linear combination of spectra corresponding to $Mn^{2+}$, $Mn^{3+}$ and $Mn^{4+}$ valence states with 3.75 % $Mn^{2+}$ and 3.75 % $Mn^{4+}$, that is, approximately one anti-Frenkel defect in every nine unit cells. The inset shows the symmetry inequivalent Er and O positions. **b**, Data points present the O K-edge in the bulk. Grey and black lines are calculated spectra for apical oxygen (O1 and O2), respectively, in a stoichiometric crystal. **c**, Yellow points present the O K-edge in the region with enhanced conductivity (the bulk spectrum (blue) is shown for reference). The black line is the calculated spectrum for planar oxygen (O3) in the presence of anti-Frenkel defects as sketched in the inset. Transitions are labelled according to the projected density of states (pDOS, Supplementary Fig. S13b). Red arrows indicate a peak at about 537 eV, which is characteristic for contributions from planar oxygen. All EELS spectra are taken on the same single line scan with even thickness and are spatially averaged over the regions indicated by the blue and yellow lines in Fig. 2b.

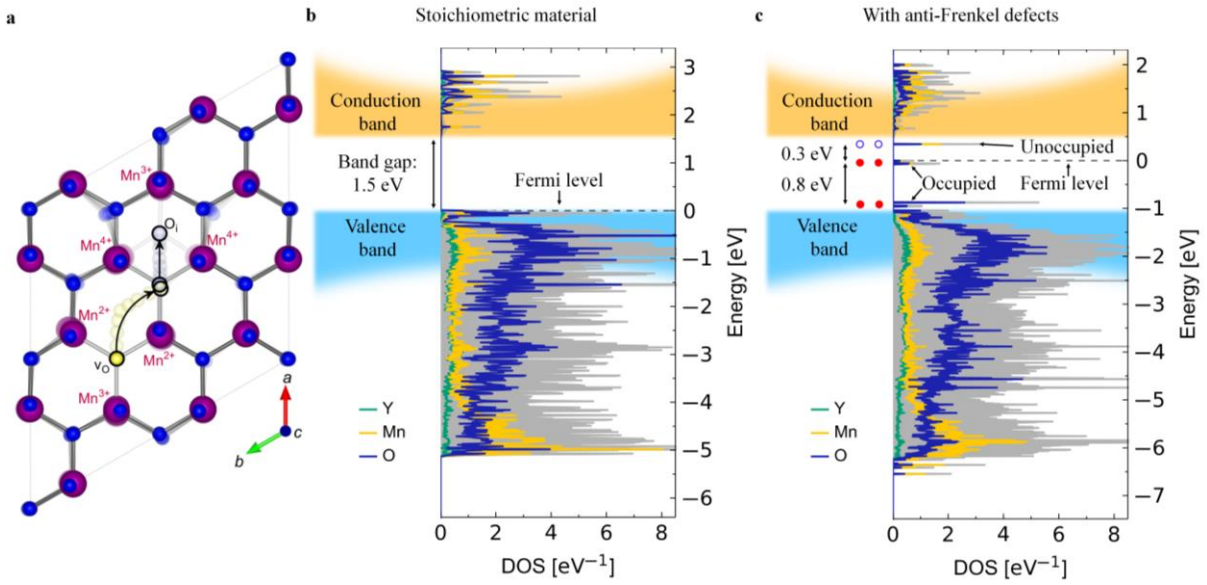


**Figure 4 | Anti-Frenkel defects and electronic density of states. a,** Formation of an anti-Frenkel defect in a 120 atom supercell. A planar lattice oxygen (yellow) is migrating from its lattice site into another planar oxygen lattice site (grey), which in turn is nudged into an interstitial site, resulting in the formation of an anti-Frenkel defect. The resulting local charge compensation of the constituting $O_i''$ and $v_O^{\bullet\bullet}$ are labelled $Mn^{4+}$ and $Mn^{2+}$, respectively. **b,** Total (grey) and atomic electronic density of states (DOS) for a stoichiometric 270 atom h-$YMnO_3$ supercell with key features schematically highlighted (valence band – light blue, conduction band – dark yellow). **c**, Same calculation for a 270 atom h-$YMnO_3$ supercell containing one anti-Frenkel defect, that is, one anti-Frenkel defect in every nine unit cells or, equivalently, 3.70 % Mn atoms in the $Mn^{4+}$ state and 3.70 % in the $Mn^{2+}$ state. Red and blue spheres in **c** schematically illustrate occupied and unoccupied defect states within the band gap.

## Methods

**Samples** High-quality single crystals are grown by the pressurised floating-zone method[44] and different samples are oriented by Laue diffraction and cut with thicknesses of ≈ 0.5 - 1 mm. The surfaces are chemo-mechanically polished with silica slurry to give a root-mean-square roughness of about 1 nm.

**Scanning probe microscopy** The SPM measurements are recorded using a NT-MDT NTEGRA Prima SPM. For all the cAFM scans we used TipsNano DCP20 probes with the voltage applied to the back of the sample. For the PFM scans we used Asylec-01-R2 Ti/Ir probes with an AC voltage amplitude of 10 V applied to the back of the sample.

**Transmission electron microscopy** TEM specimens are prepared from the middle of the conductive region using a Thermo Fisher Scientific G4 UX DualBeam FIB (Focused Ion Beam). In-situ lift-out is done with backside milling and a final polishing voltage of 2 kV. (S)TEM is performed with a double Cs corrected cold FEG JEOL ARM 200FC, operated at 200 kV and equipped with a Quantum ER GIF. High resolution high-angle-annular-dark-field scanning transmission electron microscopy (HAADF STEM) images are taken with a spatial resolution of 78 pm. The energy resolution, as determined by the FWHM of the zero loss peak, in the electron energy loss spectroscopy (EELS) is 0.5 eV. HAADF STEM images are acquired with a 27 mrad beam semi-convergence angle, inner and outer semi-collection angles of 43 and 170 mrad, and with 22 pA beam current. STEM-EELS acquisitions are performed with 120 pA beam current, 33 mrad semi-collection angle into the GIF, combined with 0.05 eV/channel energy dispersion. Dual EELS is performed to reposition the energy scale in all spectra. The EELS data in Fig. 3 is taken in a single 820 nm long line which is then split into three 200 nm wide regions, as indicated in Fig. 2, that are spatially averaged to give the spectra presented in Fig. 3. For measuring Er displacement, series of fast/short-exposure HAADF-STEM images are acquired and processed with SmartAlign[45]. Atom plane detection is done with Atomap[46] and averages are computed based on all planes.

**Density functional theory** DFT calculations are performed with the projector augmented wave (PAW) method[47] as implemented in VASP[48,49]. 3x3x1 supercells with 270 atoms are used, with expected $Mn^{2+}/Mn^{4+}$ concentrations of 3.70 %, to mimic the measured concentrations. For Y, Mn and O, 11, 11 and 6 electrons, respectively, are treated as valence electrons, with a plane-wave energy cut-off of 550 eV. Brillouin zone integration is done on a $\Gamma$-centered 1x1x2 *k*-point mesh for geometry optimizations, and on a 2x2x3 mesh for density of states (DOS) calculations. The DOS calculations have an energy resolution of 0.0067 eV/point. The non-collinear magnetic structure of the Mn sublattice is

approximated by a collinear frustrated antiferromagnetic order[50]. Experimental lattice parameters[51] and band gap[52] are reproduced using the PBEsol functional[53] and spin-polarized GGA+U[54] with a Hubbard U of 5 eV on Mn 3*d*. In defect cells ionic positions are optimized under fixed bulk lattice parameters until the forces on all ions are below 0.01 eV $Å^{-1}$. Charge corrections for charged defects in periodic boundary conditions are accounted for by extrapolation based on the Madelung potential[55]. As the electronic properties of oxygen stoichiometric[19] and non-stoichiometric[21,22] h-*R*$MnO_3$ are governed by the bonding between Mn(3d) and O(2p) states, we choose the prototypical h-$YMnO_3$ as our DFT model system to avoid f-electrons and slow convergence with Er.

**EELS simulations** A 30 atom unit cell is used as the input files in FEFF. Theoretical EELS (on approximately 115 atom clusters) spectra are simulated using the FEFF9 code[38,56] based on Green's function multiple-scattering theory where the parameters SCF (specifies the radius of the cluster for full multiple scattering during the self-consistency loop) and FMS (computes full multiple scattering within a sphere of radius r centred on the absorbing atom) are set to certain values. An SCF of 4 Å, FMS of 6 Å, and RPA screened corehole card is used for all clusters. In the EELS option card, the following values are utilized from experiment: 200 kV beam energy, collection angle of 66.9 mrad, convergence angle 27 mrad, and taken at the zone-axis [1 0 0] ($k_x$= 1, $k_y$=0, $k_z$=0). A broadening of 0.5 eV is applied to account for the finite resolution in the EELS experiment, corresponding to the FWHM of the zero-loss peak (ZLP) in the EELS spectra.

## Methods References


44. Yan, Z. *et al.* Growth of high-quality hexagonal $ErMnO_3$ single crystals by the pressurized floating-zone method. *J. Cryst. Growth* **409**, 75–79 (2015).

45. Jones, L. *et al.* Smart Align—a new tool for robust non-rigid registration of scanning microscope data. *Adv. Struct. Chem. Imaging* **1**, 8 (2015).

46. Nord, M., Vullum, P. E., MacLaren, I., Tybell, T. & Holmestad, R. Atomap: a new software tool for the automated analysis of atomic resolution images using two-dimensional Gaussian fitting. *Adv. Struct. Chem. Imaging* **3**, 9 (2017).

47. Blöchl, P. E. Projector augmented-wave method. *Phys. Rev. B* **50**, 17953–17979 (1994).

48. Kresse, G. & Furthmüller, J. Efficient iterative schemes for ab initio total-energy calculations using a plane-wave basis set. *Phys. Rev. B* **54**, 11169–11186 (1996).

49. Kresse, G. & Joubert, D. From ultrasoft pseudopotentials to the projector augmented-wave method. *Phys. Rev. B* **59**, 1758–1775 (1999).

50. Medvedeva, J. E., Anisimov, V. I., Korotin, M. A., Mryasov, O. N. & Freeman, A. J. Effect of Coulomb correlation and magnetic ordering on the electronic structure of two hexagonal phases of ferroelectromagnetic $YMnO_3$. *J. Phys. Condens. Matter* **12**, 4947–4958 (2001).

51. Gibbs, A. S., Knight, K. S. & Lightfoot, P. High-temperature phase transitions of hexagonal $YMnO_3$. *Phys. Rev. B* **83**, 94111 (2011).

52. Degenhardt, C., Fiebig, M., Fröhlich, D., Lottermoser, T. & Pisarev, R. V. V. Nonlinear optical spectroscopy of electronic transitions in hexagonal manganites. *Appl. Phys. B* **73**, 139–144 (2001).

53. Perdew, J. P. *et al.* Restoring the Density-Gradient Expansion for Exchange in Solids and Surfaces. *Phys. Rev. Lett.* **100**, 136406 (2008).

54. Dudarev, S. L., Botton, G. A., Savrasov, S. Y., Humphreys, C. J. & Sutton, A. P. Electron-energy-loss spectra and the structural stability of nickel oxide: An LSDA+U study. *Phys. Rev. B* **57**, 1505–1509 (1998).

55. Murphy, S. T. & Hine, N. D. M. Anisotropic charge screening and supercell size convergence of defect formation energies. *Phys. Rev. B* **87**, 94111 (2013).

56. Rehr, J. J. *et al.* Ab initio theory and calculations of X-ray spectra. *Comptes Rendus Phys.* **10**, 548–559 (2009).